ISSN: 2688-8645

Simulation Study of Environmentally Friendly Lead-Free All-Perovskite Tandem Solar Cells

Wei Luo *, Yan Hua, Jian Han

School of Physics and Electronic Engineering, Northeast Petroleum University, Daqing, Heilongjiang, 163318, China

* Corresponding Author: Wei Luo (Email: lwsy711@163.com)

Abstract

The toxicity of lead in perovskite solar cells has long been a significant barrier to their widespread commercialization. The improvement of environmentally friendly tandem solar cells presents the additional challenge of identifying highly efficient materials for both the wide-bandgap top cell and the narrow-bandgap bottom cell. In this study, we have reported a lead-free, non-toxic tandem perovskite solar cell , investigated through numerical simulations, by pairing an Sb^{3+}-doped double perovskite, $Cs_2AgBi_{0.75}Sb_{0.25}Br_6$, with a bandgap of 1.8 eV, as the top cell, with a tin-based $MASnI_3$ bottom cell, which has a bandgap of 1.3 eV. Upon optimization, the simulated device achieves an open-circuit voltage of 2.29 V, a current density of 15.5 mA/cm^2, and a remarkable photovoltaic conversion efficiency of 26.8%. These results are on par with the performance of state-of-the-art Pb-based tandems, highlighting the competitiveness of Pb-free materials. These simulation results highlight the potential of lead-free perovskite tandem architectures for environmentally sustainable, high-efficiency photovoltaic applications.

Keywords

Perovskite; Solar Cell; Tandem; Lead-free; Device Simulation.

1. Introduction

The emergence of perovskite solar cells (PSCs) presents a promising, low-cost photovoltaic technology with the potential to either replace or complement traditional silicon-based cells[1]. PSCs efficiency has increased dramatically within just over a decade, from 3.8% to 26.1% [2]. In addition, PSCs offer several unique advantages, such as solution-based processing, low-temperature fabrication, and a tunable bandgap[3]. The light-absorbing materials in PSCs primarily consist of perovskite compounds, which exhibit outstanding photovoltaic properties. However, High-efficiency perovskite solar cells continue to depend on lead-based materials., such as $MAPbI_3$ and $FAPbI_3$. The extreme toxicity and bioaccumulation potential of lead present serious risks to both ecosystems and human health[4], posing significant obstacles to the widespread commercialization of PSCs. As a result, one of the key areas of research in this field is the development of lead-free perovskite materials, replacing lead with non-toxic metals[5,6]. Tin (Sn), shares a similar valence electron configuration (ns^2np^2) with Pb, which allows its compounds to exhibit similar semiconductor properties. Halide tin perovskite solar cells have shown their photon conversion efficiency(PCE) reached as high as 9% after optimization. [7]. Despite their potential, the susceptibility of Sn^{2+} to oxidation and its relatively low efficiency remain significant challenges that need further attention. At the same time, in recent years, the heteroallene double perovskite structure $A_2BB'X_6$ has attracted growing research interest. Theoretical studies suggest that when the B site is occupied by Ag^+ and the B' site by Sb^{3+}, Bi^{3+}, or In^{3+}, these combinations are more resistant to air and moisture degradation, while also offering favorable processability[8,9]. However, the bandgap of $Cs_2AgB'Cl_6$ perovskites is

ISSN: 2688-8645

generally too wide, limiting their ability to effectively absorb sunlight. At the same time, $Cs_2AgB'I_6$ perovskites have shown poor stability in practical applications[10–13].The $Cs_2AgB'Br_6$ (where B' = Sb, Bi) perovskites are emerging as promising alternatives. Their wide bandgap structure makes them well-suited for tandem solar cells. Recent studies have shown that solar cells based on $Cs_2AgBiBr_6$ can achieve a PCE of around 2–3%[14]. This indicates that further research and optimization are needed for these materials. $Cs_2AgBi_{0.75}Sb_{0.25}Br_6$, used as a wide-bandgap top cell material, enhances the intrinsic properties of bismuth-based perovskites through Sb^{3+} doping. Substituting Sb at the Bi sites reduces the bandgap from 2.05 eV (indirect) to 1.8 eV (quasi-direct)[15], bringing it closer to the ideal bandgap range for top cells (1.7–1.9 eV). The bottom layer consists of a narrow-bandgap (1.3 eV) tin-based perovskite, $MASnI_3$ [16],which boasts high carrier mobility (>200 cm^2/Vs) and strong near-infrared absorption (>10^4 cm^{-1}), maximizing the capture of low-energy photons. To overcome p-type self-doping[17] and stability issues[18] caused by the oxidation of Sn^{2+}, this study utilizes cation stabilization (MA^+) to suppress degradation, ensuring the bottom cell maintains strong performance (with efficiency greater than 14%).

The Shockley–Queisser (S–Q) limit constrains the power conversion efficiency of single-junction solar cells to about 33%[19]. By stacking subcells with complementary bandgaps, tandem architectures more fully exploit the solar spectrum and thus offer a pathway to surpass this theoretical ceiling. This approach significantly reduces thermalization and transmission losses[20]. Lead-based perovskite tandem cells have achieved a certified efficiency of 33.9%[21]. In contrast, lead-free perovskite single-junction cells generally exhibit low efficiencies (<15%) [22], and there is a lack of highly efficient matching tandem systems, slowing the progress of lead-free tandem cells. Developing material systems that combine an ideal bandgap, high stability, and low toxicity is a critical challenge in advancing high-efficiency lead-free tandem solar cells.

Research indicates that achieving high efficiency in tandem photovoltaic devices depends critically on bandgap selection. The top cell performs best when its bandgap lies between 1.7 and 1.9 eV. For the bottom cell, the optimal bandgap is in the range of 0.9 to 1.2 eV. The Eperon team led the way in developing a fully tandem PSCs with ideal bandgap matching in a monolithic double-junction structure, achieving a PCE of 17% , an open-circuit voltage (V_{OC}) of 1.65 V [23]. Additionally, the Forács group experimentally demonstrated that bilayer all-PSCs with dual-terminal monolithic integration can achieve an average PCE of 15%[24]. Rajagopal's research team reported a tandem all-PSC with a PCE of 18.5% and a remarkably V_{OC} of 1.98 V [25]. In addition, the McMeekin team experimentally demonstrated that the steady-state efficiency of double-junction all-PSCs exceeded 15%. Through photovoltaic modeling simulations, the team also predicted that devices employing the most advanced structures could theoretically achieve a PCE of 26.7% [26].

Tandem PSCs remain in the initial phase of development. In our study, we conducted comprehensive optimization simulations of tandem all-PSCs, with a particular focus on addressing lead toxicity concerns throughout the process. We selected the lead-free perovskite material $Cs_2AgBi_{0.75}Sb_{0.25}Br_6$(1.8 eV), and the bottom subcell used $MASnI_3$ as absorber layer. First, we identified suitable electron transport layer (ETL) and hole transport layer (HTL) materials based on absorption layer parameters from experimental literature. Next, we simulated how changing the absorption layers thicknesses in both subcells independently affected photovoltaic parameters and external quantum efficiency (EQE). From these results, we determined the optimal thicknesses for the absorber layers of both subcells. The bottom subcell was modeled under the spectrum transmitted through the perovskite layer. We then optimized the thicknesses of both subcells to achieve current matching, yielding the tandem device's optimal performance metrics. This work does not aim to predict near-term

ISSN: 2688-8645

experimentally achievable efficiencies, but to provide design guidelines under constrained assumptions

2. Device Structure and Method

In this study, the photovoltaic performance of PSCs was numerically simulated using the one-dimensional solar cell simulation software SCAPS-1D (Solar Cell Capacitance Simulator, developed by ELIS at Ghent University, Belgium)[27]. Since SCAPS-1D supports direct modeling of up to seven-layer structures, a stepwise approach was employed to simulate tandem PSC. First, the photovoltaic performance of the subcells was independently optimized. Then, the top subcell's output spectrum was used as the incident spectrum for the bottom subcell, thereby characterizing their optical coupling and current-matching properties within the actual tandem structure. The software utilizes these following equations [28][29]:

$$\nabla \cdot \varepsilon \nabla \varphi = -q(p - n + N_D - N_A) \quad (1)$$

Here, ε is the dielectric permittivity of the semiconductor medium, φ denotes the electrostatic potential. The constant q represents the elementary charge. The n and p are carrier densities for electrons and holes. The terms N_D and N_A correspond to the concentrations of ionized donor and acceptor species.

Continuity Equation for Charge Carrier Drift-Diffusion Model:

$$J_n = qn\mu_n E + qD_n \frac{\partial n}{\partial x} \quad (2)$$

$$J_p = qn\mu_p E - qD_p \frac{\partial n}{\partial x} \quad (3)$$

In this context, the mobilities of electrons and holes are denoted by μ_n and μ_p, respectively, whereas their diffusion coefficients are represented by D_n and D_p. The equations above describe two key types of currents—drift and diffusion currents. Here, The carrier charge is denoted by q, the electric field by E, and the electron and hole concentrations by n and p.

In this study, We investigated two perovskite absorbers—$Cs_2AgBi_{0.75}Sb_{0.25}Br_6$ (1.8 eV) and $MASnI_3$ (1.3 eV)—for top and bottom subcell structures. The material properties of $Cs_2AgBi_{0.75}Sb_{0.25}Br_6$ and $MASnI_3$ were derived from the existing literature[11,16]. For the top subcell, we used phenyl-C_{61}-butyric acid methyl ester (PCBM) for the ETL and copper(II) oxide (Cu_2O) for the HTL. Due to the optimal bandgap alignment with $Cs_2AgBi_{0.75}Sb_{0.25}Br_6$. In a similar approach, the 1.3 eV bottom subcell was constructed using zinc oxide (ZnO) and copper iodide (CuI) as the ETL and HTL. The structures of the tandem PSC are depicted in **Figure 1**. Specifically, the top subcell structure is FTO (40 nm)/PCBM (40 nm)/$Cs_2AgBi_{0.75}Sb_{0.25}Br_6$ (600 nm, unless otherwise specified)/Cu_2O (50 nm), while the bottom subcell consists of ZnO (50 nm)/$MASnI_3$ (450 nm, unless otherwise specified)/CuI (100 nm).

Figure 1 illustrates the structural layout and spectral properties of a tandem PSC design, utilizing the top subcells(1.8eV) and the bottom subcells(1.3 eV), respectively. In monolithic tandem configurations, the tunnel recombination junction plays a key role. It ensures that the short-circuit current (JSC) remains identical for both the top and bottom subcells. For the tandem design analysis, the subcells were simulated independently, a widely adopted approach in studies using SCAPS-1D, where tandem performance is evaluated through current matching[30,31]. In this scheme, the AM1.5G spectrum was directed onto the top subcell, with the transmitted light subsequently driving the bottom subcell, leading to current matching in the tandem structure[32]. Because the program cannot explicitly model tunnel recombination layers, the connection between the top and bottom subcells was approximated as an ideal tunnel junction. The transmission spectrum incident on the bottom subcell, as filtered through the top subcell, is described by Equation (4).

ISSN: 2688-8645

$$S(\lambda) = S_0(\lambda) \times \exp\left(\sum_{i=1}^{4} -(\alpha_{Mi}(\lambda) \times d_{Mi})\right) \quad (4)$$

Here, $S_0(\lambda)$ denotes the incident AM 1.5 spectrum, λ is the wavelength, α is the absorption coefficient, and d denotes the thicknesses of the constituent layers in the perovskite top cell. Mi refers to FTO, PCBM, perovskite, and Cu_2O.

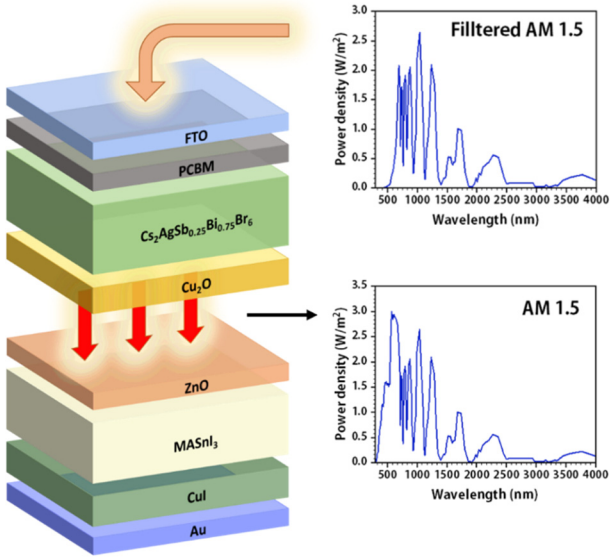

Figure 1. (Schematic representation of the tandem all-PSCs used in simulation. The top subcell is illuminated by the AM1.5 spectrum, and the transmitted spectrum is used to simulate the photovoltaic response of the bottom subcell.)

Table 1 are provide the electrical properties and defect densities of the materials employed in the simulations. **Figure 2** shows the band diagrams for all layers used in the simulations of the tandem PSCs. The optical properties, including the absorption coefficients, are presented in **Figure 3**.

Table 1. (The material properties for the perovskite and the parameters for the HTL and ETL used in the simulations.)

Parameters	FTO[33]	ZnO[34]	PCBM[35]	$Cs_2AgBi_{0.75}Sb_{0.25}Br_6$ [35]	$MASnI_3$ [16]	CuI [36]	Cu_2O' [37]
Bandgap(eV)	3.5	3.3	2	1.8	1.3	3.1	2.17
Electron affinity(eV)	4	4	3.9	3.58	4.17	2.1	3.2
Dielectric permittivity	9	9	4	6.5	10	6.5	7.11
CB effective density of states(cm^{-3})	2.2×10^{18}	3.7×10^{18}	1×10^{21}	2.2×10^{18}	1.5×10^{19}	2.8×10^{19}	2×10^{17}
VB effective density of states(cm^{-3})	1.8×10^{18}	1.8×10^{19}	2×10^{20}	1.8×10^{19}	1.47×10^{18}	1×10^{19}	1×10^{19}
Electron mobility(cm^2/Vs)	20	100	0.01	2	2	100	20
Hole mobility(cm^2/Vs)	10	25	0.01	2	2	43.9	80
Donor density(cm^{-3})	1×10^{19}	1×10^{18}	1×10^{15}	1×10^{13}	1×10^{15}		
Acceptor density (cm^{-3})		1×10^{15}		1×10^{17}	1×10^{15}	1×10^{18}	1×10^{18}
Number of defect density(N_t)	1×10^{15}	1×10^{15}	1×10^{15}	1×10^{15}	1×10^{15}	1×10^{15}	1×10^{15}

ISSN: 2688-8645

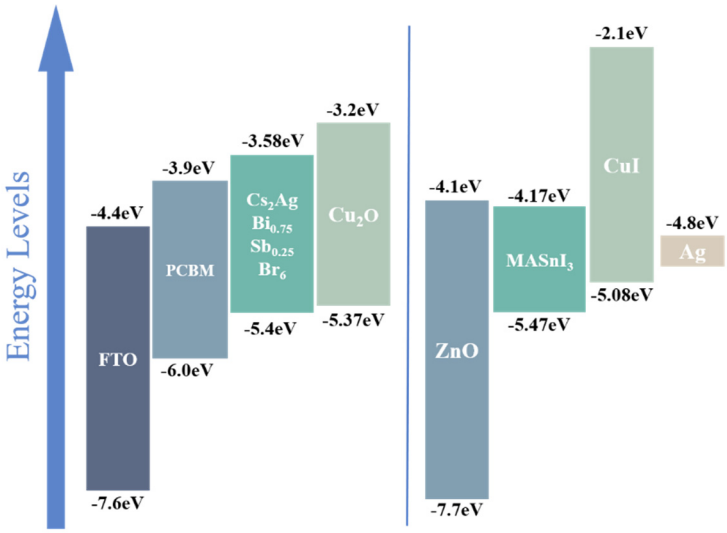

Figure 2. (Band diagrams for all layers used in simulating the two solar cells.)

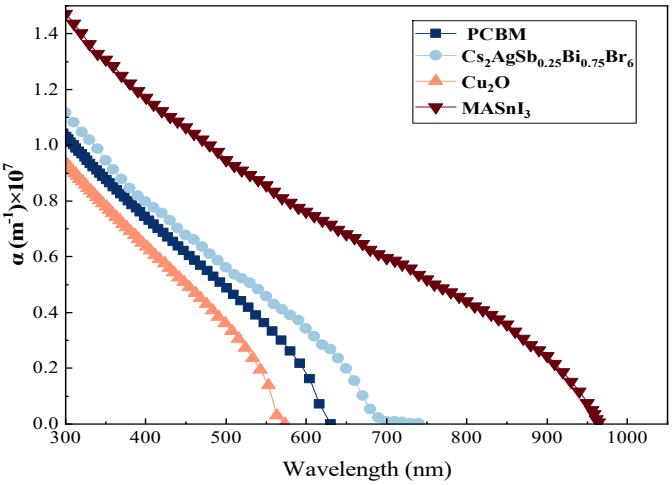

Figure 3. *(*Absorption coefficients *of $Cs_2AgBi_{0.75}Sb_{0.25}Br_6$, PCBM, Cu_2O, and $MASnI_3$ used in the* simulation *to calculate the filtered spectrum.)*

3. Results and Discussion

3.1. Calibration of the Top and Bottom Subcells

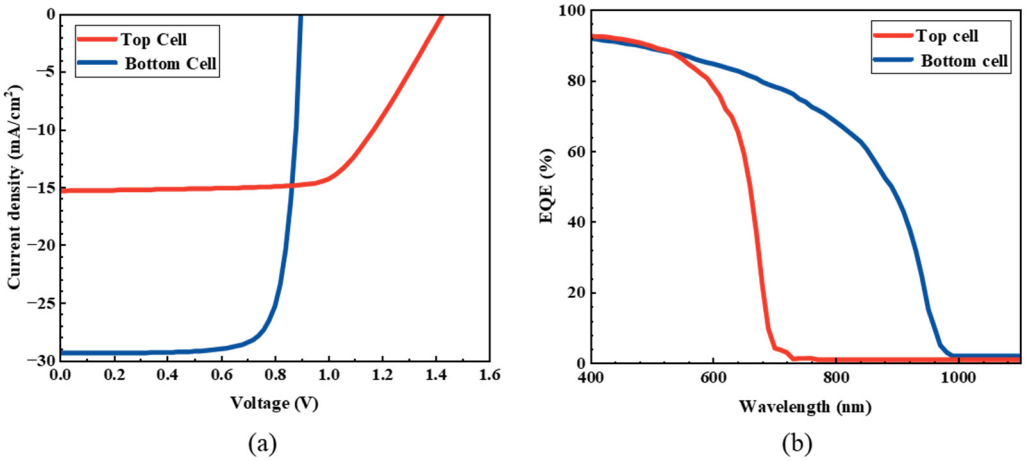

Figure 4. *(**(a)** Photovoltaic J-V curves for the top and bottom subcells operating independently. **(b)** EQE curves for the top and bottom subcells operating independently.)*

ISSN: 2688-8645

Figure 4(a) display the simulated current density-voltage (J-V) curves ,The EQE displayed in **4(b)**. The J_{SC} values are 15.74 mA/cm^2 in the top subcells and 32.3 mA/cm^{2}in the bottom subcells, with V_{OC} of 1.425 V and 0.884 V. At a wavelength of 400 nm, both subcells show an EQE of 90%. For the top subcell, the EQE sharply declines to 0% for wavelengths longer than 600 nm, while the bottom subcell exhibits strong absorption in the 600–1000 nm range.

Figure 5 (a-b) show the both subcells band diagrams operating independently under open-circuit conditions. The top wide-bandgap subcell demonstrates significant electron-hole quasi-Fermi level separation, driven by strong band bending in its absorber layer. This behavior aligns with the perovskite built-in electric field optimization strategy described by McMeekin et al[38]. In contrast, the bottom narrow-bandgap subcell shows a slightly lower electron-hole quasi-Fermi level separation (≈0.86 eV) due to its narrower bandgap. However, the pronounced band tilts at the interfaces of the transport layers (0–50 nm and 450–550 nm) suggest that optimized energy level matching between the HTL and ETL reduces interfacial recombination[39]. Both subcells exhibit a stepped band alignment at the interconnection region (around 500 nm), facilitating efficient tunneling of photo-generated electrons from the top to the bottom subcell, get a total V_{OC} of 2.29 V.

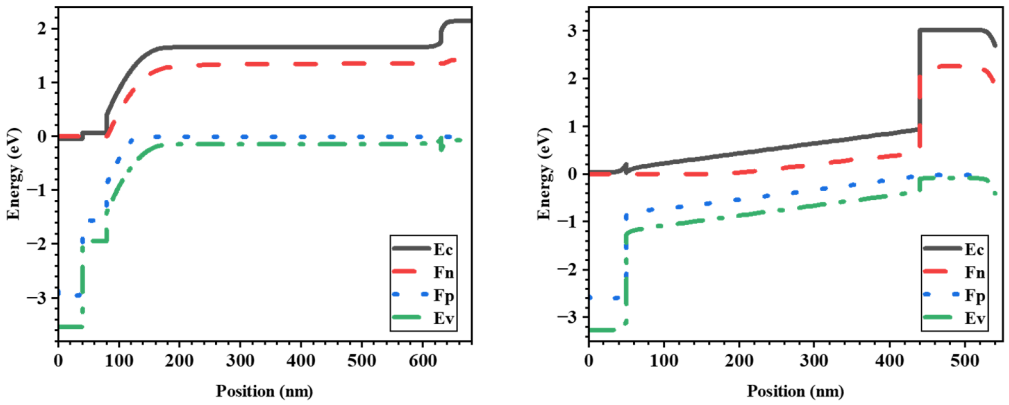

Figure 5. *(**(a)** Band diagram of the top cell and **(b)** band diagram of the bottom cell under open-circuit conditions)*

3.2. Effect of Absorber Layer Thickness on Top and Bottom Subcell Performance under Isolated Conditions

We investigated the impact of the absorber layer thickness on the performance of the top and bottom subcells separately before analyzing the performance of tandem all-PSCs. **Figures 6(a-d)** shows the J-V curves and EQE of the absorber layers at varying thicknesses in the top and bottom subcells, respectively.

As shown in **Figures 6(a)** and **(c)**, the J_{SC} increases significantly with thickness, owing to enhanced absorption and the generation of more electron-hole pairs. However, beyond a thickness of 600 nm, the J_{SC} levels off. This is because the increase of the cell thickness result in the photogenerated electrons and holes diffuse over a longer distance to reach the electrode, which increases the likelihood of recombination losses. The dark saturation current rises with thickness, which leads to higher recombination losses, ultimately reducing V_{OC} at higher thicknesses. This relationship is clearly demonstrated by Equation (5) below:

$$V_{oc} = \frac{kT}{q} \ln\left(\frac{J_{sc}}{J_0} + 1\right) \quad (5)$$

In the equation, kT/q represents the thermal voltage, and J_0 denotes the reverse saturation current density.

ISSN: 2688-8645

Therefore, J_{SC} and EQE are most effectively optimized at lower absorber thicknesses. As the thickness increases, their values gradually reach saturation. For the top cell, when the absorber layer thicknesses were 5×10^1 nm, 1×10^2 nm, 1.5×10^2 nm, and 2×10^2 nm, the J_{SC} values were 6.39 mA/cm^2, 8.70 mA/cm^2, 10.50 mA/cm^2, and 11.91 mA/cm^2, respectively. A similar increase in J_{SC} was observed as the absorber layer thicknesses were varied in the bottom subcell.

Figures 6(b) and **6(d)** demonstrate that increasing the absorber layer thickness leads to notable improvements in EQE. The EQE curve of the device exhibited a pronounced upward trend with increasing thickness, following the same pattern observed in the J-V characteristics. However, beyond the optimized thickness, the increase in the EQE spectrum gradually saturates. This is because high-energy photons (short wavelengths), which have a high absorption coefficient, are rapidly absorbed at the front surface of the device. In contrast, low-energy photons (long wavelengths), with a lower absorption coefficient, show a slower increase in absorption efficiency as the thickness increases. As a result, further increases in thickness produce only marginal improvements in EQE. This effect is especially pronounced in the long-wavelength region.

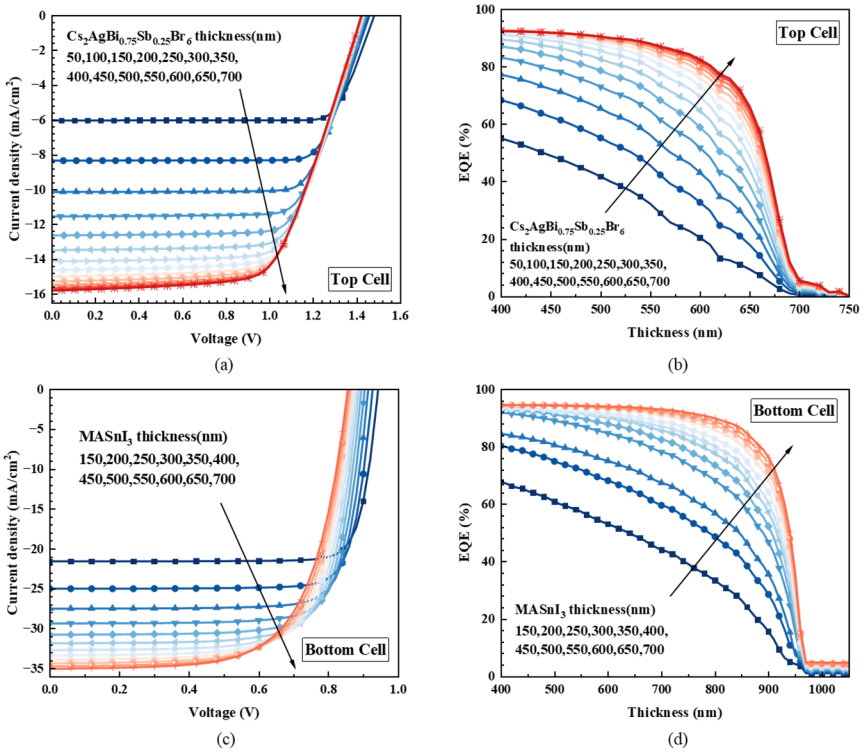

Figure 6. *(**(a)** J-V curves of the top cell as the* absorber *layer thickness increases. **(b)** EQE curves of the top cell as the absorber layer thickness increases. **(c)** J-V curves of the bottom cell as the absorber layer thickness increases. **(d)** EQE curves of the bottom cell as the absorber layer thickness increases.)*

Figure 7(a) and **(b)** illustrate how the photovoltaic parameters of the top and bottom absorbers vary with thickness. As observed, V_{OC} and fill factor (FF) decrease with increasing absorber thickness, while J_{SC} and PCE increase with thickness. However, the PCE saturates at higher thicknesses, specifically at the top cell(600 nm) and the bottom cell(500nm). Since carrier mobility tends to decrease with increasing film thickness, the FF consequently decreases as well. The FF is calculated using Equation (6) [40]:

$$FF=\frac{P_{max}}{V_{oc}\times I_{sc}} \tag{6}$$

ISSN: 2688-8645

Where $P_{max} = V_{mpp} \times I_{mpp}$, corresponding to the maximum power output, calculated as the product of current and voltage at the maximum power point.

From the above equation, it is evident that as V_{OC} decreases, J_{SC} approaches saturation, and FF also decreases correspondingly.

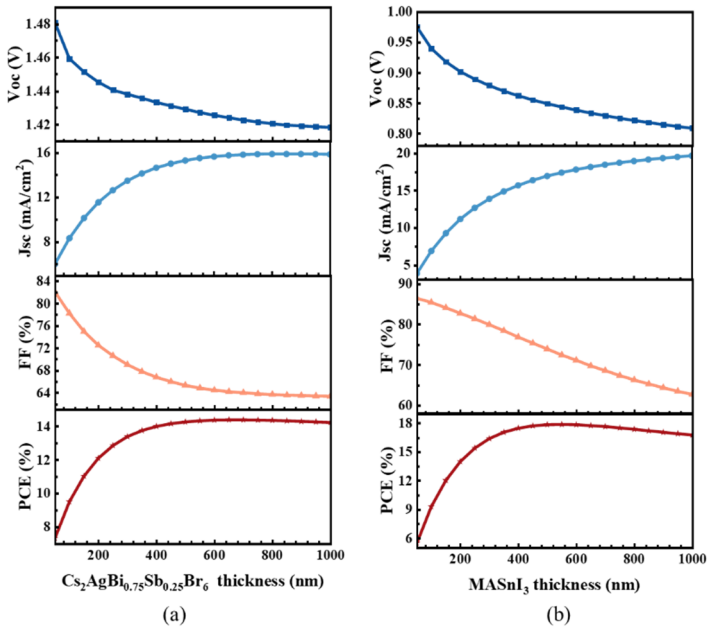

Figure 7. *(**(a)** Variation of top cell photovoltaic* parameters *with absorption layer thickness.* ***(b)*** *Variation of bottom cell photovoltaic parameters with absorption layer thickness.)*

3.3. Influence of the Defect Density

The density of bulk defects in the absorber layer plays a central role in non-radiative recombination and the associated voltage losses in lead-free PSCs. For emerging Pb-free perovskite absorbers, however, reported defect densities span a broad range across the literature. To avoid drawing conclusions that depend on a single assumed value, device performance was examined over a representative range of absorber defect densities.

Figure 8 summarizes the evolution of the key photovoltaic parameters with increasing defect density for both the top and bottom subcells. In both cases, the V_{OC} decreases monotonically as the defect density increases, consistent with progressively enhanced recombination losses from electrically active defects. By contrast, the J_{SC} is only weakly affected at low defect densities, but declines more rapidly at higher values, indicating that carrier collection becomes increasingly limited once recombination dominates. The FF follows a similar downward trend, reflecting the combined impact of recombination and transport losses.

Consequently, the PCE decreases continuously with increasing defect density. This efficiency loss is governed primarily by the reduction in V_{OC}, whereas the contributions from J_{SC} and FF become significant only at elevated defect densities. Although both subcells exhibit the same qualitative behavior, the bottom subcell shows a more pronounced overall degradation.

On the basis of these results, a bulk defect density of 1×10^{13} to 1×10^{17}cm^{-3} was selected for subsequent simulations. At this value, the devices retain stable electrical characteristics and avoid excessive recombination-induced losses, while remaining within a defect-density range widely regarded as achievable for lead-free perovskite absorbers. This choice strikes a balance between physical realism and numerical robustness, and enables a meaningful comparison of device architectures without relying on overly optimistic assumptions.

ISSN: 2688-8645

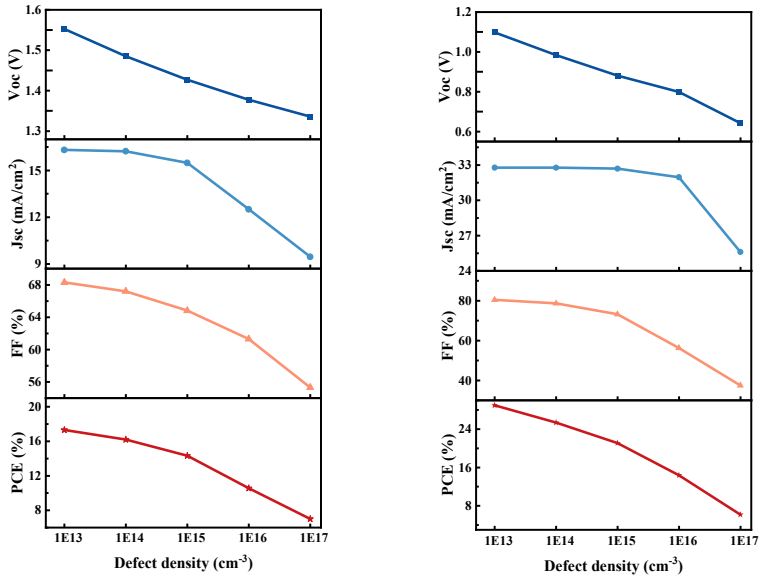

Figure 8. *(Dependence of the V_{OC}, J_{SC}, FF, and PCE on the defect density of the absorber layer for* ***(a)*** *the top subcell and* ***(b)*** *the bottom subcell.)*

3.4. Two-terminal All-perovskite Tandem Solar Cell

In this section, we integrate theboth subcells studied earlier into a tandem structure (details of the specific structure and method are provided in Part II). The filtered spectrum for the bottom cell is obtained using Equation (4) from the previous section, along with the absorption coefficients of each layer in the top cell For optimal performance in double-junction tandem PSCs, current matching is crucial. This is because, in a tandem configuration, the two subcells function like series-connected diodes, necessitating equal current flow through both. Therefore, their respective photocurrent densities must be precisely matched. Additionally, for tandem architectures, the total V_{OC} drop corresponds to the sum of the V_{OC} drops across all subcells. Accordingly, the overall J_{SC} is limited by the lower current density[32,41,42]. In a series-connected configuration, optimizing the performance of both the top and bottom cells, while ensuring their J_{SC} values are precisely matched, is crucial for achieving the best PCE. This matching is essential to facilitate efficient current flow through the series structure, including through the tunnel junction[41,43,44].

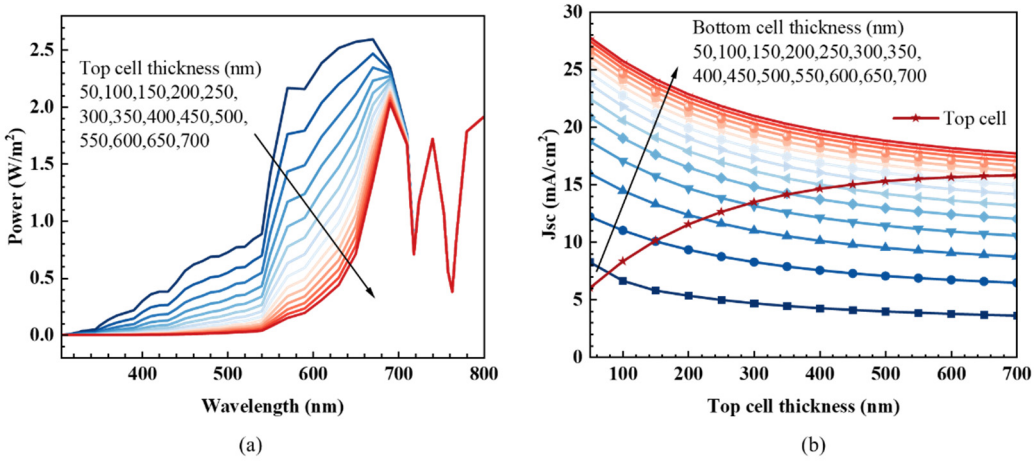

Figure 9. *(****(a)*** *AM1.5G* spectral *transmittance of light passing through top cells with varying perovskite thicknesses (50–700 nm).* ***(b)*** *Variation in J_{SC} of the top cell and bottom cell with perovskite layer thickness(50nm-500nm))*

ISSN: 2688-8645

Figure 1 illustrates the illumination spectra of the top and bottom subcells in the tandem device. The top subcell was first simulated with absorber thicknesses ranging from 50 to 700 nm, while all other layer thicknesses were kept constant. The resulting filtered transmission spectrum of the top subcell was calculated and is shown in **Figure 9(a)**. Simulation results reveal that the transmission spectral intensity decreases significantly as the absorber layer thickness increases, since thicker layers absorb incident light more efficiently. The resulting filtered spectra were employed as the illumination for the bottom subcell in the simulations.

Figure 9(b) presents the J_{SC} values for the subcells under various combinations of absorber layer thicknesses within the tandem structure. The figure demonstrates that optimal current matching is obtained with an absorber thickness combination of 550 nm(top subcell) and 390 nm(bottom subcell).,yielding J_{SC} values of 15.55 and 15.50 mA/cm^2, respectively.

Building on the previous current matching analysis, we systematically examined how the photovoltaic parameters of the bottom subcell vary with different combinations of the absorber layer thicknesses under filtered spectral irradiation. The results are presented as contour plots in **Figure 10(a–d)**.

The J_{SC} of the bottom subcell decreases significantly as the top subcell thickness increases are shown in **Figure 10(a)**. This behavior arises because the enhanced suppression of incident light by thicker top absorber layers, which reduces the photon flux reaching the bottom subcell. In contrast to J_{SC}, the V_{OC} of the bottom subcell shows little variation with changes in the top subcell thickness, as shown in **Figure 10(b)**. The bottom subcell get a higher FF when the absorber layer is thinner, owing to reduced series resistance. However, as shown in **Figure 10(c)**, FF gradually decreases progressively with increasing bottom absorber thickness. Under filtered spectral conditions, the PCE of the bottom subcell is influenced by the combined effects of J_{SC}, V_{OC}, and FF, with its variation trend shown in **Figure 10(d)**.

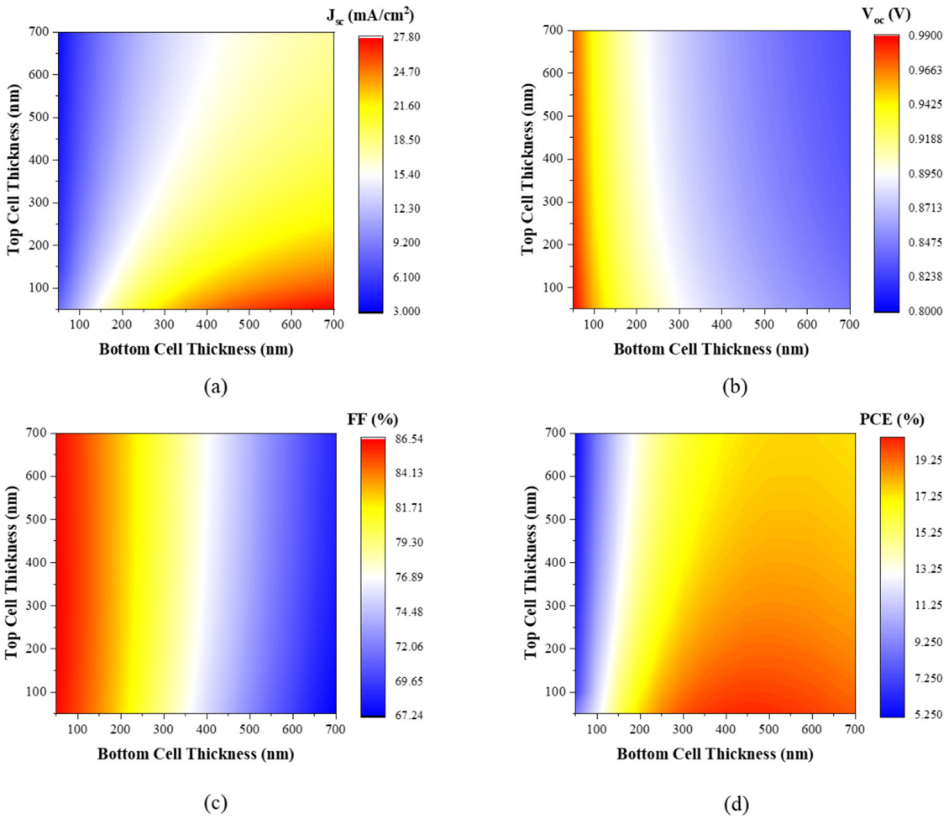

***Figure 10**. (Contour plots of photovoltaic parameters for the bottom subcell with varying top and bottom absorber layer thicknesses: **(a)** J_{SC}, **(b)** V_{OC}, **(c)** FF, **(d)** PCE.)*

ISSN: 2688-8645

Under current-matching conditions with the top subcell, the bottom subcell achieved a PCE of 17.4%, a V_{OC} of 0.86 V, an FF of 77.1%, and a J_{SC} of 15.5 mA/cm^2. For each point of equal current density, the voltages of the two subcells were summed to construct the tandem J–V curve. the corresponding voltage values of the two subcells are summed to synthesize the tandem device J-V curve[32].

Figure 11(a) displays the J–V curves of the independent top and bottom subcells alongside the resulting curve of the current-matched tandem device. The J–V curve of the tandem solar cell alone is presented in **Figure 11(b)**. The photovoltaic parameters of the device are listed in **Table** 2. Tandem all-PSCs were simulated under the current-matching conditions described above.

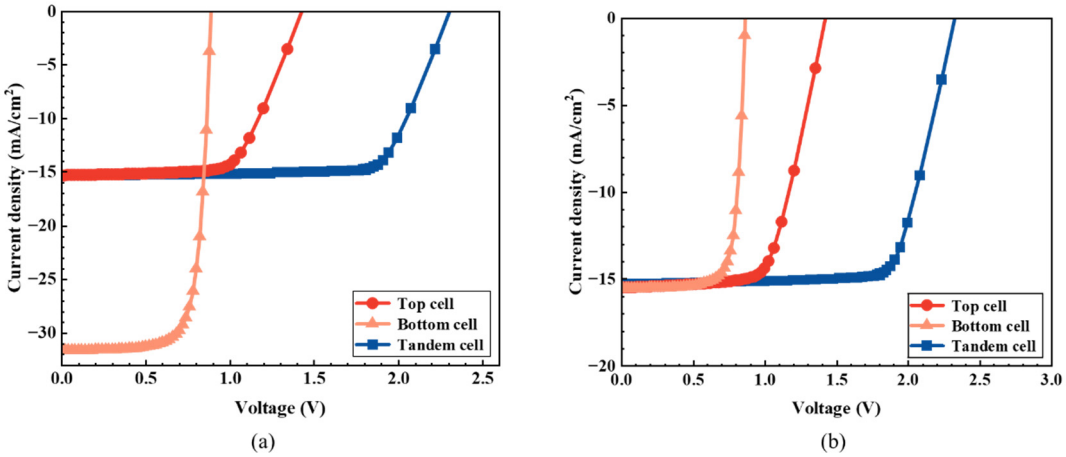

Figure 11. *(**(a)** J-V curves of the standalone top cell, standalone bottom cell, and series-connected cells. **(b)** J-V curves of the top cell, bottom cell, and series-connected cells after illumination with filtered spectra.)*

Table 2. *(PV parameters of the top cell, bottom cell, and series-connected cells after illumination with filtered spectra.)*

cell	V_{oc}(V)	J_{sc}(mA/cm^2)	FF(%)	PCE(%)
Top Cell	1.43	15.5	64.82	14.32
Bottom cell	0.86	15.5	77.1	17.4
Tandem Cell	2.29	15.5	75.3	26.8

As shown in the table, the top and bottom subcells yield identical JSC values after irradiation with the filtered spectrum. This indicates that the current matching condition is satisfied in the series-connected configuration. The V_{OC} of the series-connected cells is the sum of the top and bottom subcells, which are 1.43 V and 0.86 V, respectively. Similarly, the PCE of the series-connected cell is 26.8%, while the FF of 75.3% was calculated using the formula (8) presented earlier.

4. Conclusion

In this study, we propose and develop a fully lead-free two-terminal tandem perovskite solar cell. The top subcell absorber is the double-perovskite $Cs_2AgBi_{0.75}Sb_{0.25}Br_6$ (bandgap 1.8 eV), while the bottom subcell employs $MASnI_3$ with a bandgap of 1.3 eV. We optimized the thicknesses of the absorber and HTL/ETL layers in both perovskite systems.The PCE of the top subcell reached 14.33%, while the bottom subcell achieved 21.1%. A defect density of 10^{15} cm^{-3} was incorporated into the model to improve the reliability of the simulations. The top subcell

ISSN: 2688-8645

was illuminated with the typical AM1.5G spectrum, and light filtered through the top subcell was directed onto the bottom subcell. Optimal current matching was established by carefully adjusting their thicknesses to satisfy the current continuity requirement of the tandem structure. The tandem device exhibited maximum performance with top and bottom absorber layers of 550 nm and 390 nm, resulting in PCEs of 14.33% and 17.4% for the respective subcells. The tandem cell J–V characteristics were obtained by summing the voltages of the subcells at equal current. In this study, the parameters of the tandem cell used are as follows: V_{OC} (2.29V) , J_{SC} (15.5mA/cm^2) , FF(75.3%) , PCE(26.8%).

This simulation study provides valuable insights into designing highly efficient, non-toxic all-PSCs, identifying optimal layer thicknesses and corresponding ETL/HTL configurations. While current dual-perovskite materials still face challenges, such as limited stability, and simulations cannot fully replicate the complex variables encountered in experiments, this theoretical modeling offers a clear strategy for optimizing the performance of high-efficiency, lead-free all-PSCs. Future research should focus on refining the material system and improving the model to address these existing limitations.

Acknowledgments

All the authors would like to thank Prof. Marc Burgelman (University of Gent, Belgium) for providing the SCAPS-1D software. This work was financially supported by the Hainan Engineering Research Center for Virtual Reality Technology and Systems (QiongfaGaigaoji [2023] No.818) and Key Research and Development Project of Hainan Province (ZDYF2022 GXjS220).

References

[1] Grätzel, M. The Light and Shade of Perovskite Solar Cells. *Nat. Mater.* **2014**, *13* (9), 838–842. https:// doi. org/10.1038/nmat4065.

[2] Hicks, W. Best Research-Cell Efficiency Chart, 2025. https://www.nrel.gov/pv/cell-efficiency.

[3] Jeong, J.; Kim, M.; Seo, J.; Lu, H.; Ahlawat, P.; Mishra, A.; Yang, Y.; Hope, M. A.; Eickemeyer, F. T.; Kim, M.; Yoon, Y. J.; Choi, I. W.; Darwich, B. P.; Choi, S. J.; Jo, Y.; Lee, J. H.; Walker, B.; Zakeeruddin, S. M.; Emsley, L.; Rothlisberger, U.; Hagfeldt, A.; Kim, D. S.; Grätzel, M.; Kim, J. Y. Pseudo-Halide Anion Engineering for α-FAPbI3 Perovskite Solar Cells. *Nature* **2021**, *592* (7854), 381–385. https:// doi. org/ 10.1038/s41586-021-03406-5.

[4] Babayigit, A.; Duy Thanh, D.; Ethirajan, A.; Manca, J.; Muller, M.; Boyen, H.-G.; Conings, B. Assessing the Toxicity of Pb- and Sn-Based Perovskite Solar Cells in Model Organism Danio Rerio. *Sci. Rep.* **2016**, *6* (1), 18721. https://doi.org/10.1038/srep18721.

[5] Lyu, M.; Yun, J.-H.; Cai, M.; Jiao, Y.; Bernhardt, P. V.; Zhang, M.; Wang, Q.; Du, A.; Wang, H.; Liu, G.; Wang, L. Organic–Inorganic Bismuth (III)-Based Material: A Lead-Free, Air-Stable and Solution-Processable Light-Absorber beyond Organolead Perovskites. *Nano Res.* **2016**, *9* (3), 692–702. https://doi.org/10.1007/s12274-015-0948-y.

[6] Zhu, H. X.; Liu, J.-M. Electronic Structure of Organometal Halide Perovskite CH3NH3BiI3 and Optical Absorption Extending to Infrared Region. *Sci. Rep.* **2016**, *6* (1), 37425. https://doi. org/10. 1038/ srep37425.

[7] Sahoo, G.; Polaki, S. R.; Pazhedath, A.; Krishna, N. G.; Mathews, T.; Kamruddin, M. Synergetic Effect of NiO_x Decoration and Oxygen Plasma Treatment on Electrochemical Capacitor Performance of Vertical Graphene Nanosheets. *ACS Appl. Energy Mater.* **2021**, *4* (1), 791–800. https://doi. org/10. 1021/ acsaem.0c02683.

[8] Slavney, A. H.; Hu, T.; Lindenberg, A. M.; Karunadasa, H. I. A Bismuth-Halide Double Perovskite with Long Carrier Recombination Lifetime for Photovoltaic Applications. *J. Am. Chem. Soc.* **2016**, *138* (7), 2138–2141. https://doi.org/10.1021/jacs.5b13294.

[9] Kangsabanik, J.; Sugathan, V.; Yadav, A.; Yella, A.; Alam, A. Double Perovskites Overtaking the Single Perovskites: A Set of New Solar Harvesting Materials with Much Higher Stability and Efficiency. *Phys. Rev. Mater.* **2018**, *2* (5), 055401. https://doi.org/10. 1103/ PhysRev Materials.2.055401.

[10] Zhao, X.-G.; Yang, D.; Sun, Y.; Li, T.; Zhang, L.; Yu, L.; Zunger, A. Cu–In Halide Perovskite Solar Absorbers. *J. Am. Chem. Soc.* **2017**, *139* (19), 6718–6725. https://doi.org/10.1021/jacs.7b02120.

[11] McClure, E. T.; Ball, M. R.; Windl, W.; Woodward, P. M. Cs_2 $AgBiX_6$ (X = Br, Cl): New Visible Light Absorbing, Lead-Free Halide Perovskite Semiconductors. *Chem. Mater.* **2016**, *28* (5), 1348–1354. https://doi.org/10.1021/acs.chemmater.5b04231.

[12] Filip, M. R.; Hillman, S.; Haghighirad, A. A.; Snaith, H. J.; Giustino, F. Band Gaps of the Lead-Free Halide Double Perovskites Cs_2 $BiAgCl_6$ and Cs_2 $BiAgBr_6$ from Theory and Experiment. *J. Phys. Chem. Lett.* **2016**, *7* (13), 2579–2585. https://doi.org/10.1021/acs.jpclett.6b01041.

[13] Volonakis, G.; Haghighirad, A. A.; Milot, R. L.; Sio, W. H.; Filip, M. R.; Wenger, B.; Johnston, M. B.; Herz, L. M.; Snaith, H. J.; Giustino, F. Cs_2 $InAgCl_6$: A New Lead-Free Halide Double Perovskite with Direct Band Gap. *J. Phys. Chem. Lett.* **2017**, *8* (4), 772–778. https://doi.org/10.1021/acs.jpclett.6b02682.

[14] Noman, M.; Khan, Z.; Jan, S. T. A Comprehensive Review on the Advancements and Challenges in Perovskite Solar Cell Technology. *RSC Adv.* **2024**, *14* (8), 5085–5131. https://doi. org/10. 1039/ D3RA07518D.

[15] Meyer, E.; Mutukwa, D.; Zingwe, N.; Taziwa, R. Lead-Free Halide Double Perovskites: A Review of the Structural, Optical, and Stability Properties as Well as Their Viability to Replace Lead Halide Perovskites. *Metals* **2018**, *8* (9), 667. https://doi.org/10.3390/met8090667.

[16] Pandey, R.; Bhattarai, S.; Sharma, K.; Madan, J.; Al-Mousoi, A. K.; Mohammed, M. K. A.; Hossain, M. K. Halide Composition Engineered a Non-Toxic Perovskite–Silicon Tandem Solar Cell with 30.7% Conversion Efficiency. *ACS Appl. Electron. Mater.* **2023**, *5* (10), 5303–5315. https://doi.org/10. 1021/ acsaelm.2c01574.

[17] Nakamura, T.; Yakumaru, S.; Truong, M. A.; Kim, K.; Liu, J.; Hu, S.; Otsuka, K.; Hashimoto, R.; Murdey, R.; Sasamori, T.; Kim, H. D.; Ohkita, H.; Handa, T.; Kanemitsu, Y.; Wakamiya, A. Sn(IV)-Free Tin Perovskite Films Realized by in Situ Sn(0) Nanoparticle Treatment of the Precursor Solution. *Nat. Commun.* **2020**, *11* (1), 3008. https://doi.org/10.1038/s41467-020-16726-3.

[18] Urbain, F.; Smirnov, V.; Becker, J.-P.; Lambertz, A.; Yang, F.; Ziegler, J.; Kaiser, B.; Jaegermann, W.; Rau, U.; Finger, F. Multijunction Si Photocathodes with Tunable Photovoltages from 2.0 V to 2.8 V for Light Induced Water Splitting. *Energy Environ. Sci.* **2016**, *9* (1), 145–154. https:// doi. org/ 10. 1039/C5EE02393A.

[19] Shockley, W.; Queisser, H. J. Detailed Balance Limit of Efficiency of P-n Junction Solar Cells.

[20] Al-Ashouri, A.; Köhnen, E.; Li, B.; Magomedov, A.; Hempel, H.; Caprioglio, P.; Márquez, J. A.; Morales Vilches, A. B.; Kasparavicius, E.; Smith, J. A.; Phung, N.; Menzel, D.; Grischek, M.; Kegelmann, L.; Skroblin, D.; Gollwitzer, C.; Malinauskas, T.; Jošt, M.; Matič, G.; Rech, B.; Schlatmann, R.; Topič, M.; Korte, L.; Abate, A.; Stannowski, B.; Neher, D.; Stolterfoht, M.; Unold, T.; Getautis, V.; Albrecht, S. Monolithic Perovskite/Silicon Tandem Solar Cell with >29% Efficiency by Enhanced Hole Extraction. *Science* **2020**, *370* (6522), 1300–1309. https://doi.org/10.1126/science.abd4016.

[21] Liu, J.; Chen, X.; Chen, K.; Tian, W.; Sheng, Y.; She, B.; Jiang, Y.; Zhang, D.; Liu, Y.; Qi, J.; Chen, K.; Ma, Y.; Qiu, Z.; Wang, C.; Yin, Y.; Zhao, S.; Leng, J.; Jin, S.; Zhao, W.; Qin, Y.; Su, Y.; Li, X.; Li, X.; Zhou, Y.; Zhou, Y.; Ling, F.; Mei, A.; Han, H. Electron Injection and Defect Passivation for High-Efficiency Mesoporous Perovskite Solar Cells. *Science* **2024**, *383* (6688), 1198–1204. https://doi.org/10. 1126/ science. adk9089.

[22] Ke, W.; Kanatzidis, M. G. Prospects for Low-Toxicity Lead-Free Perovskite Solar Cells. *Nat. Commun.* **2019**, *10* (1), 965. https://doi.org/10.1038/s41467-019-08918-3.

[23] Eperon, G. E.; Leijtens, T.; Bush, K. A.; Prasanna, R.; Green, T.; Wang, J. T.-W.; McMeekin, D. P.; Volonakis, G.; Milot, R. L.; May, R.; Palmstrom, A.; Slotcavage, D. J.; Belisle, R. A.; Patel, J. B.; Parrott, E. S.; Sutton, R. J.; Ma, W.; Moghadam, F.; Conings, B.; Babayigit, A.; Boyen, H.-G.; Bent, S.; Giustino, F.; Herz, L. M.; Johnston, M. B.; McGehee, M. D.; Snaith, H. J. Perovskite-Perovskite Tandem Photovoltaics with Optimized Band Gaps. *Science* **2016**, *354* (6314), 861–865. https://doi. org/ 10. 1126/ science.aaf9717.

[24] Forgács, D.; Gil-Escrig, L.; Pérez-Del-Rey, D.; Momblona, C.; Werner, J.; Niesen, B.; Ballif, C.; Sessolo, M.; Bolink, H. J. Efficient Monolithic Perovskite/Perovskite Tandem Solar Cells. *Adv. Energy Mater.* **2017**, *7* (8), 1602121. https://doi.org/10.1002/aenm.201602121.

[25] Rajagopal, A.; Yang, Z.; Jo, S. B.; Braly, I. L.; Liang, P.; Hillhouse, H. W.; Jen, A. K. -Y. Highly Efficient Perovskite–Perovskite Tandem Solar Cells Reaching 80% of the Theoretical Limit in Photovoltage. *Adv. Mater.* **2017**, *29* (34), 1702140. https://doi.org/10.1002/adma.201702140.

[26] McMeekin, D. P.; Mahesh, S.; Noel, N. K.; Klug, M. T.; Lim, J.; Warby, J. H.; Ball, J. M.; Herz, L. M.; Johnston, M. B.; Snaith, H. J. Solution-Processed All-Perovskite Multi-Junction Solar Cells. *Joule* **2019**, *3* (2), 387–401. https://doi.org/10.1016/j.joule.2019.01.007.

[27] Burgelman, M.; Nollet, P.; Degrave, S. Modelling Polycrystalline Semiconductor Solar Cells. *Thin Solid Films* **2000**, *361–362*, 527–532. https://doi.org/10.1016/S0040-6090(99)00825-1.

[28] Duan, Q.; Ji, J.; Hong, X.; Fu, Y.; Wang, C.; Zhou, K.; Liu, X.; Yang, H.; Wang, Z.-Y. Design of Hole-Transport-Material Free CH3NH3PbI3/CsSnI3 All-Perovskite Heterojunction Efficient Solar Cells by Device Simulation. *Sol. Energy* **2020**, *201*, 555–560. https://doi.org/10. 1016/j.solener. 2020. 03. 037.

[29] Li, S.; Liu, P.; Pan, L.; Li, W.; Yang, S.-E.; Shi, Z.; Guo, H.; Xia, T.; Zhang, S.; Chen, Y. The Investigation of Inverted P-i-n Planar Perovskite Solar Cells Based on FASnI3 Films. *Sol. Energy Mater. Sol. Cells* **2019**, *199*, 75–82. https://doi.org/10.1016/j.solmat.2019.04.023.

[30] Gupta, G. K.; Dixit, A. Theoretical Studies of Single and Tandem Cu2ZnSn(S/Se)4 Junction Solar Cells for Enhanced Efficiency. *Opt. Mater.* **2018**, *82*, 11–20. https://doi.org/ 10.1016/ j. optmat. 2018. 05. 030.

[31] Kim, K.; Gwak, J.; Ahn, S. K.; Eo, Y.-J.; Park, J. H.; Cho, J.-S.; Kang, M. G.; Song, H.-E.; Yun, J. H. Simulations of Chalcopyrite/c-Si Tandem Cells Using SCAPS-1D. *Sol. Energy* **2017**, *145*, 52–58. https:// doi. org/ 10. 1016/j.solener.2017.01.031.

[32] Burdick, J.; Glatfelter, T. Spectral Response and I–V Measurements of Tandem Amorphous-Silicon Alloy Solar Cells. *Sol. Cells* **1986**, *18* (3–4), 301–314. https://doi.org/10.1016/0379-6787(86) 901 29-8.

[33] Abdelaziz, S.; Zekry, A.; Shaker, A.; Abouelatta, M. Investigating the Performance of Formamidinium Tin-Based Perovskite Solar Cell by SCAPS Device Simulation. *Opt. Mater.* **2020**, *101*, 109738. https:// doi.org/10.1016/j.optmat.2020.109738.

[34] Hossain, M. K.; Rubel, M. H. K.; Toki, G. F. I.; Alam, I.; Rahman, Md. F.; Bencherif, H. Effect of Various Electron and Hole Transport Layers on the Performance of $CsPbI_3$ -Based Perovskite Solar Cells: A Numerical Investigation in DFT, SCAPS-1D, and wxAMPS Frameworks. *ACS Omega* **2022**, *7* (47), 43210–43230. https://doi.org/10.1021/acsomega.2c05912.

[35] Madan, J.; Shivani; Pandey, R.; Sharma, R. Device Simulation of 17.3% Efficient Lead-Free All-Perovskite Tandem Solar Cell. *Sol. Energy* **2020**, *197*, 212–221. https://doi.org/ 10.1016/ j. solener. 2020. 01.006.

[36] Kanoun, A.-A.; Kanoun, M. B.; Merad, A. E.; Goumri-Said, S. Toward Development of High-Performance Perovskite Solar Cells Based on CH3NH3GeI3 Using Computational Approach. *Sol. Energy* **2019**, *182*, 237–244. https://doi.org/10.1016/j.solener.2019.02.041.

[37] Chatterjee, S.; Pal, A. J. Introducing Cu_2 O Thin Films as a Hole-Transport Layer in Efficient Planar Perovskite Solar Cell Structures. *J. Phys. Chem. C* **2016**, *120* (3), 1428–1437. https:// doi.org/ 10. 1021/ acs.jpcc.5b11540.

[38] McMeekin, D. P.; Sadoughi, G.; Rehman, W.; Eperon, G. E.; Saliba, M.; Hörantner, M. T.; Haghighirad, A.; Sakai, N.; Korte, L.; Rech, B.; Johnston, M. B.; Herz, L. M.; Snaith, H. J. A Mixed-Cation Lead Mixed-Halide Perovskite Absorber for Tandem Solar Cells. *Science* **2016**, *351* (6269), 151–155. https:// doi. org/10.1126/science.aad5845.

[39] Deng, Y.; Xu, S.; Chen, S.; Xiao, X.; Zhao, J.; Huang, J. Defect Compensation in Formamidinium–Caesium Perovskites for Highly Efficient Solar Mini-Modules with Improved Photostability. *Nat. Energy* **2021**, *6* (6), 633–641. https://doi.org/10.1038/s41560-021-00831-8.

[40] Green, M. A. *Solar Cells: Operating Principles, Technology, and System Applications*; 1982.

ISSN: 2688-8645

[41] Chen, B.; Yu, Z.; Liu, K.; Zheng, X.; Liu, Y.; Shi, J.; Spronk, D.; Rudd, P. N.; Holman, Z.; Huang, J. Grain Engineering for Perovskite/Silicon Monolithic Tandem Solar Cells with Efficiency of 25.4%. *Joule* **2019**, *3* (1), 177–190. https://doi.org/10.1016/j.joule.2018.10.003.

[42] Shankar, G.; Kumar, P.; Pradhan, B. All-Perovskite Two-Terminal Tandem Solar Cell with 32.3% Efficiency by Numerical Simulation. *Mater. Today Sustain.* **2022**, *20*, 100241. https://doi.org/ 10. 1016/j.mtsust.2022.100241.

[43] Sahli, F.; Werner, J.; Kamino, B. A.; Bräuninger, M.; Monnard, R.; Paviet-Salomon, B.; Barraud, L.; Ding, L.; Diaz Leon, J. J.; Sacchetto, D.; Cattaneo, G.; Despeisse, M.; Boccard, M.; Nicolay, S.; Jeangros, Q.; Niesen, B.; Ballif, C. Fully Textured Monolithic Perovskite/Silicon Tandem Solar Cells with 25.2% Power Conversion Efficiency. *Nat. Mater.* **2018**, *17* (9), 820–826. https://doi.org/10.1038/s41563-018-0115-4.

[44] Abdelaziz, S.; Zekry, A.; Shaker, A.; Abouelatta, M. Investigation of Lead-Free MASnI3-MASnIBr2 Tandem Solar Cell: Numerical Simulation. *Opt. Mater.* **2022**, *123*, 111893. https://doi.org/ 10. 1016/ j.optmat.2021.111893.